arXiv:cond-mat/9808038v2 [cond-mat.mes-hall] 8 Jul 1999

Semiclassical theory of surface plasmons in spheroidal clusters

A. Dellafiore[a], F. Matera[b,a] and F. A. Brieva[c]
[a]) *Istituto Nazionale di Fisica Nucleare, Sezione di Firenze,*
[b]) *Dipartimento di Fisica, Università degli Studi di Firenze,*
L.go E. Fermi 2, I-50125, Firenze, Italy
[c]) *Departamento de Física, Facultad de Ciencias Físicas y Matemáticas,*
Universidad de Chile, Casilla 487–3, Santiago, Chile

Abstract

A microscopic theory of linear response based on the Vlasov equation is extended to systems having spheroidal equilibrium shape. The solution of the linearized Vlasov equation, which gives a semiclassical version of the random phase approximation, is studied for electrons moving in a deformed equilibrium mean field. The deformed field has been approximated by a cavity of spheroidal shape, both prolate and oblate. Contrary to spherical systems, there is now a coupling among excitations of different multipolarity induced by the interaction among constituents. Explicit calculations are performed for the dipole response of deformed clusters of different size. In all cases studied here the photoabsorption strength for prolate clusters always displays a typical double-peaked structure. For oblate clusters we find that the high–frequency component of the plasmon doublet can get fragmented in the medium size region ($N \sim 250$). This fragmentation is related to the presence of two kinds of three-dimensional electron orbits in oblate cavities. The possible scaling of our semiclassical equations with the valence electron number and density is investigated.

PACS: 36.40.Gk, 36.40.Mr

I. INTRODUCTION

Complex many-fermion systems like atomic clusters and nuclei exhibit both spherical and deformed equilibrium shapes. Deformation of the ground state gives rise to observable effects in the excitation spectrum of these systems, with the splitting of the giant dipole resonance in deformed nuclei most likely being the best well known feature [1]. Based on the close analogy that exists between the nuclear giant dipole resonance and the cluster surface plasmon, a similar splitting is expected and has indeed been observed in atomic clusters (see Refs. [2] and [3] for reviews of experimental and theoretical work). A spheroidal deformation (prolate and oblate) is often sufficient to explain data in both nuclei and atomic clusters although recent jellium model calculations [4] also suggest more complicated shapes for the latter.

Clemenger [5] has used a deformed oscillator model, which is inspired by the Nilsson model of nuclear physics [6], to describe deformed clusters. However Strutinsky *et al.* [7] have pointed out that the oscillator potential is somewhat special and argued that a spheroidal cavity would give a more realistic description of the equilibrium mean field (in nuclei, but the same is true for large atomic clusters). Actually the spheroidal cavity is still a rather special choice since its sharp surface is an undesirable feature. A mean field with a diffuse surface would be more realistic. Studies by Arvieu *et al.* [8] of the classical motion of a particle in a deformed Saxon–Woods like potential indicate that part of the classical phase space becomes chaotic. In a spheroidal cavity instead the single-particle motion is integrable and this fact makes calculations practicable.

In this paper we study surface plasmons in deformed clusters by assuming a spheroidal cavity model for the equilibrium mean field. Thus we limit our analysis to the simplest deviation from spherical shape and consider only spheroidal geometry. However our model is not limited to small deformations and, in principle, we can study systems ranging from spherical to almost cigar or disk-like shapes. Our aim is to extend the semiclassical theory of linear response based on the Vlasov equation of Refs. [9,10] to deformed systems. This theory can be viewed as a semiclassical version of the random phase approximaton (RPA). Although a fully quantum treatment of the problem is certainly more rigorous, the Vlasov equation has the advantage that the numerical effort required is greatly reduced. Indeed, a fully quantum RPA calculation for finite systems must rely heavily on numerical computation. This fact has limited explicit calculations mostly to either infinite homogeneous or spherical systems, where the symmetries of the mean field Hamiltonian allow for simplifications of the numerical problem. Pioneering work on the quantum response of spheroidal clusters has been made by Ekardt and Penzar [11] (for prolate clusters only).

The present work is organized as follows. In Sect. II we extend the formalism of Refs. [9,10] to spheroidal systems. In order to present clearly the main points of the theory we have relegated the discussion of many detailed expressions to the Appendix. In Sect. III the model is applied to study the evolution of the peak profile of surface plasmons with deformation. Both the "single-particle" and collective responses are studied for prolate and oblate geometries. Finally, Sect. IV contains a brief summary and the conclusions.

II. FORMALISM

In spite of its well known difficulties in reproducing the observed width of collective resonances, the RPA is still the basic microscopic theory of small–amplitude vibrations for many fermions systems. The RPA theory can be derived in the Green function formalism [12]. The RPA Green function G obeys an integral equation that can be written formally as

$$G(\omega) = G^0(\omega) + G^0(\omega) V G(\omega) \, , \tag{2.1}$$

where the unperturbed particle-hole Green function G^0 describes the single-particle motion of the constituents in the equilibrium mean field, and V is the effective two-body residual interaction. The response of the many-body system to a weak periodic external field of frequency ω is proportional to the imaginary part of $G(\omega)$. In practice, the calculation of G from Eq. (2.1) means facing two main problems: first to evaluate G^0 for the system under study and then solving the corresponding integral equation to determine G. The latter becomes quite a challenge when the system is non–spherical since G will be determined by a system of coupled integral equations, as we shall discuss later on.

The problem of calculating G^0 for a given mean field is simpler in the semiclassical theory of linear response developed in Refs. [9,10]. This theory has been applied to the study of giant resonances in spherical nuclei [13] and of surface plasmon excitations in spherical microclusters [14]. The excitation spectra given by this semiclassical theory are very similar to those yielded by the fully quantum RPA theory even when the many-body system under investigation is not particularly large. Moreover for large deformations it is expected (Ref. [6], p.591) that shell effects should be smaller than for spherical systems, thus favouring a semiclassical approach.

The semiclassical theory of linear response based on the Vlasov equation of Refs. [9,10] leads to an expression for the propagator with the same structure as the quantum RPA given by Eq. (2.1). However the RPA equation is actually more complicated when exchange (Fock) terms are properly taken into account [12]. Nevertheless, these terms are often treated in a local approximation leading to the same Hartee–like structure as the Vlasov equation. In the classical limit, G and G^0 will be denoted by D and D^0 respectively in order to distinguish them from the corresponding quantum quantities.

Although the theory of Refs. [9,10] is generally valid for all integrable mean field Hamiltonians, practical applications have been limited to spherical systems. In order to extend its range of application to deformed systems we consider the classical limit of Eq. (2.1) in momentum space,

$$D(\mathbf{q}',\mathbf{q},\omega) = D^0(\mathbf{q}',\mathbf{q},\omega) + \frac{1}{(2\pi)^3}\int d\mathbf{k}\, D^0(\mathbf{q}',\mathbf{k},\omega)\, V(k)\, D(\mathbf{k},\mathbf{q},\omega)\,. \tag{2.2}$$

Following [9,10], and using units $\hbar = c = 1$, the propagator D^0 can be written in terms of action–angle variables $\{\mathbf{I},\mathbf{\Phi}\}$ as

$$D^0(\mathbf{q}',\mathbf{q},\omega) = (2\pi)^3 \sum_{\mathbf{n}} \int d\mathbf{I}\, F'(h_0(\mathbf{I}))\, \frac{\mathbf{n}\cdot\boldsymbol{\omega}(\mathbf{I})}{\mathbf{n}\cdot\boldsymbol{\omega}(\mathbf{I}) - (\omega + i\varepsilon)}\, Q^*_{\mathbf{n}}(\mathbf{q}',\mathbf{I})\; Q_{\mathbf{n}}(\mathbf{q},\mathbf{I})\,, \tag{2.3}$$

with $\varepsilon \longrightarrow 0$, and the Fourier coefficients

$$Q_{\mathbf{n}}(\mathbf{q},\mathbf{I}) = \frac{1}{(2\pi)^3}\int d\mathbf{\Phi}\, e^{-i\mathbf{n}\cdot\mathbf{\Phi}}\, e^{i\mathbf{q}\cdot\mathbf{r}}\,, \tag{2.4}$$

taking the place of the quantum matrix elements (see also [15]). In Eq. (2.3), $\mathbf{n}$ is a three-dimensional vector with integer components and the sum extends to all possible values of $\mathbf{n}$. The components of the vector $\boldsymbol{\omega}$ are the fundamental frequencies of the multiply–periodic particle motion in the equilibrium mean field,

$$\boldsymbol{\omega}(\mathbf{I}) = \nabla_I h_0(\mathbf{I})\,, \tag{2.5}$$

with $h_0 = E$ the equilibrium Hamiltonian. The function $F'(E)$ in Eq. (2.3) is the derivative of

$$F(E) = \frac{2}{(2\pi\hbar)^3}\,\theta(E_F - E)\,, \tag{2.6}$$

which describes the equilibrium distribution of electrons at zero temperature (E_F is the Fermi energy). Thus,

$$F'(E) = -\frac{2}{(2\pi\hbar)^3}\,\delta(E_F - E)\,, \tag{2.7}$$

expression that reduces by one the number of integrals in Eq. (2.3). We also note that the propagator in Eq. (2.3) is perfectly well behaved when $\mathbf{n}\cdot\boldsymbol{\omega} \to 0$ due to the presence of the $\mathbf{n}\cdot\boldsymbol{\omega}$ factor in the numerator. Then D^0 is not affected by the problem of small divisors (Ref. [16], p.523).

For a realistic mean field the frequencies $\boldsymbol{\omega}$ do depend upon the value of the action variables $\mathbf{I}$. This dependence reflects the non-linearity of the mean field. A cavity is an example where this non-linearity effect is present. Instead, for the oscillator potential model where the equilibrium Hamiltonian is given by

$$(\,h_0\,)^{osc} = \boldsymbol{\omega}\cdot\mathbf{I}\,, \tag{2.8}$$

the frequencies $\boldsymbol{\omega}$ do not depend on $\mathbf{I}$. This difference is a basic distinction between the oscillator and more realistic models and it becomes the main reason for our choice to study the cavity model.

The most general partial–wave expansion of the propagator $D^0(\mathbf{q}',\mathbf{q},\omega)$ is

$$D^0(\mathbf{q}',\mathbf{q},\omega) = \sum_{LM}\sum_{L'M'} D^0_{LM,L'M'}(q',q,\omega) Y_{L'M'}(\hat{\mathbf{q}}')Y^*_{LM}(\hat{\mathbf{q}})\,. \tag{2.9}$$

The symmetry properties of the system allow for a simplification of this expression. Indeed, the axial symmetry of spheroidal (and also spherical) systems implies

$$D^0_{LM,L'M'} = \delta_{M,M'} D^0_{L'LM}(q',q,\omega)\,, \tag{2.10}$$

and therefore

$$D^0(\mathbf{q}',\mathbf{q},\omega) = \sum_{L=0}^{\infty}\sum_{M=-L}^{L}\sum_{L'=|M|}^{\infty} D^0_{L'LM}(q',q,\omega) Y_{L'M}(\hat{\mathbf{q}}')Y^*_{LM}(\hat{\mathbf{q}})\,. \tag{2.11}$$

A similar expansion for the propagator $D(\mathbf{q}',\mathbf{q},\omega)$ is obtained from Eq. (2.2). Thus, for spheroidal systems, the three–dimensional integral equation (Eq. (2.2)) reduces to the following system of coupled one–dimensional integral equations for the coefficients $D_{L'LM}(q',q,\omega)$,

$$\begin{aligned} D_{L'LM}(q',q,\omega) = {} & D^0_{L'LM}(q',q,\omega) \\ & + \frac{1}{(2\pi)^3}\sum_{\ell=|M|}^{\infty}\int_0^{\infty} dk\, k^2 D^0_{L'\ell M}(q',k,\omega)V(k)D_{\ell LM}(k,q,\omega)\,. \end{aligned} \tag{2.12}$$

This equation can be further simplified for spherical symmetry. In this case,

$$D^0_{L'LM}(q',q,\omega) = \delta_{L,L'} D^0_L(q',q,\omega) \qquad (\text{any } M)\,, \tag{2.13}$$

and Eq. (2.12) reduces to a single uncoupled one–dimensional integral equation for each partial–wave component,

$$D_L(q',q,\omega) = D^0_L(q',q,\omega) + \frac{1}{(2\pi)^3}\int_0^\infty dk\, k^2 D^0_L(q',k,\omega)V(k)D_L(k,q,\omega)\,. \qquad (2.14)$$

The solution of this equation for surface plasmons in spherical clusters has been studied in Ref. [14], where the coefficients $D^0_L(q',q,\omega)$ have been explicitly derived (see also Ref. [10]).

In order to solve the system of coupled integral equations expressed by Eq. (2.12), we must derive an explicit expression for the coefficients $D^0_{L'LM}(q',q,\omega)$. This can be done in a way similar to that followed in Ref. [9]. We refer here to the Appendix for details on how to extend that approach to both prolate and oblate geometries. From Eqs. (2.3) and (2.11) we obtain

$$\begin{aligned} D^0_{L'LM}(q',q,\omega) = &-\frac{2}{(2\pi\hbar)^3}\sum_{n_u,n_v}(2\pi)^3\int d\lambda_z\int d\epsilon\left|\frac{\partial(I_v,I_u)}{\partial(E,\epsilon)}\right| \\ &\times\frac{n_u\omega_u+n_v\omega_v+M\omega_\varphi}{n_u\omega_u+n_v\omega_v+M\omega_\varphi-(\omega+i\varepsilon)} \\ &\times Q^{(L'M)*}_{n_u,n_v,M}(E,\epsilon,\lambda_z;q')\,Q^{(LM)}_{n_u,n_v,M}(E,\epsilon,\lambda_z;q)\,, \end{aligned} \qquad (2.15)$$

where we have used the constants of motion $\{E,\epsilon,\lambda_z\}$ instead of the action variables $\mathbf{I}$ to evaluate the corresponding integrals. All vector quantities in Eqs.(2.3) and (2.15) are expressed through their (u,v,φ) components as discussed in the Appendix. Furthermore, the integrand is evaluated at the Fermi energy E_F as a consequence of Eq. (2.7). All other integrals are extended to the classically available phase space, the integration limits are specified in the Appendix.

The Fourier coefficients $Q^{(LM)}_{n_u,n_v,M}(E,\epsilon,\lambda_z;q)$ are related to those of Eq. (2.4) by

$$Q_{\mathbf{n}}(\mathbf{q},\mathbf{I}) = \sum_{LM} Q^{(LM)}_{\mathbf{n}} Y^*_{LM}(\hat{\mathbf{q}}), \qquad (2.16)$$

and

$$\begin{aligned} Q^{(LM)}_{n_u,n_v,n_\varphi} = &\frac{1}{\pi}\,\delta_{M,n_\varphi}\oint du\oint dv\left|\frac{\partial(\Phi_u,\Phi_v)}{\partial(u,v)}\right| e^{-i(n_u\Phi_u+n_v\Phi_v+n_\varphi\tilde{\Phi}_\varphi)} \\ &\times i^L\,Y_{LM}(\theta(u,v),0)\,j_L(qr(u,v))\,. \end{aligned} \qquad (2.17)$$

The symbol $\oint$ means integration over a whole period of classical motion in the respective variable, the angle variable Φ_φ takes the form $\Phi_\varphi = \tilde{\Phi}_\varphi(u,v)+\varphi$ and j_L is the spherical Bessel function of order L.

The comparison of Eqs.(2.12) and (2.14) explicitly shows that, contrary to the spherical case, there is a coupling between excitations of different multipolarity in deformed systems. It can be shown (see Appendix) that $D^0_{L'LM}=0$ unless $(-)^{L'}=(-)^L$, so that only multipoles with the same parity are mixed in Eq. (2.12). Since this is a consequence of the reflection symmetry of the spheroid ($z\to -z$), it holds both for prolate and oblate shapes. Such a simplification would not necessarily occur for "pear-shaped" systems.

The physical observables we consider in this work are related to the "forward" propagator $D(\mathbf{q},\mathbf{q},\omega)$ regardless of the need for the full off–diagonal propagator $D(\mathbf{q}',\mathbf{q},\omega)$ to solve

Eq. (2.2). Moreover, for randomly oriented clusters, we must average over the solid angle [1]. Thus we define the angle-averaged propagator

$$< D(q,\omega) > \equiv \frac{1}{4\pi} \int d\hat{\mathbf{q}}\, D(\mathbf{q},\mathbf{q},\omega) \, . \tag{2.18}$$

The expansion of $D(\mathbf{q}',\mathbf{q},\omega)$ analogous to Eq. (2.11) implies

$$< D(q,\omega) > = \frac{1}{4\pi} \sum_{LM} D_{LLM}(q,q,\omega) \, . \tag{2.19}$$

A quantity often used in cluster physics is the dynamic polarizability $\alpha(\omega)$. It is related to the longwavelength limit of the $L = 1$ component of $< D(q,\omega) >$. For deformed clusters the polarizability is a tensor since the induced dipole moment depends on the orientation of the cluster relative to the external field. We introduce the M–component polarizability as

$$\alpha_M(\omega) = -\,\tfrac{1}{3}\, e^2 \lim_{q\to 0} \left\{ \frac{1}{4\pi} \, \frac{D_{11M}(q,q,\omega)}{[\, j_1(q)\,]^2} \right\} \, . \tag{2.20}$$

In the spherical limit α_M is M–independent. For spheroidal systems $\alpha_{-M} = \alpha_M$ (this is a property of the coefficients $D_{L'LM}$).

We introduce also the "partial" photoabsorption cross sections

$$\sigma_M(\omega) = \frac{4\pi}{c}\, \omega\, \mathrm{Im}\, [\, \alpha_M(\omega)\,] \ , \tag{2.21}$$

and the total photoabsorption cross section is [11]

$$\sigma(\omega) = \tfrac{1}{3} \sum_{M=-1}^{1} \sigma_M(\omega) = \tfrac{1}{3}\, [\, \sigma_0(\omega) + 2\, \sigma_1(\omega)\,] \ . \tag{2.22}$$

III. RESULTS

In this section we apply the formalism developed in Sect. II and in the Appendix to the study of prolate and oblate clusters with varying degree of deformation. Also we explore the possibility of scaling with the number of valence electrons and cluster density. The emphasis is on understanding how the collective response is altered when the clusters under investigation do not have a spherical shape. We shall not attempt to compare our results with experimental data at this level of development. For this reason we do not consider such refinements as the electron "spill out" which is well known to give a red shift of the plasmon peak in spherical clusters. We expect to find a similar effect in the deformed case. No particular effort is made to reproduce the observed width of the plasmon resonances which is considerably larger than that obtained in the present model.

The picture we have in mind here corresponds to taking a spherical cluster and then deforming it to either a prolate or oblate shape while keeping its volume and density constant. We consider initially a relatively large sodium cluster of spherical shape, with $N = 254$ valence electrons, described approximately by a square-well mean-field potential of radius

$R = r_s\, N^{\frac{1}{3}}$ and r_s is the Wigner-Seitz parameter in units of the Bohr radius. We will take $r_s = 4.0$. In this case the surface plasmon resonance consists of a single peak situated near the Mie frequency,

$$\omega_{Mie} = \frac{\omega_p}{\sqrt{3}}\,, \tag{3.1}$$

with ω_p the bulk plasmon frequency. Then, this sodium cluster is deformed to a spheroidal (prolate or oblate) shape characterized by a deformation parameter η,

$$\eta = \frac{R_>}{R_<}\,, \tag{3.2}$$

where $R_>$ ($R_<$) are the larger (smaller) diameters of the spheroids. We study the changes that are expected in the distribution of the dipole strength and report results for $1 \leq \eta \leq 2$. The spherical limit is obtained by taking $\eta = 1.001$.

To describe the spheroidal systems we introduce spheroidal coordinates $\{u, v, \varphi\}$ as described in the Appendix for the prolate and oblate geometries. Assuming that electrons move in a static cavity of spheroidal shape, the equilibrium Hamiltonian h_0 will be chosen to be

$$h_0(u, v, \varphi, p_u, p_v, p_\varphi) = K(u, v, \varphi, p_u, p_v, p_\varphi) + \mathcal{V}(v)\,, \tag{3.3}$$

where $\{p_u, p_v, p_\varphi\}$ are the corresponding conjugate momenta, K is the kinetic energy and $\mathcal{V}$ the potential energy for particles in a cavity. All the calculations have been performed within this framework. The central objective has been to calculate the collective D_{11M} function from Eq. (2.12). The number of coupled integral equations required is 3 for the cases of larger deformation ($\eta = 2$) considered in this work (that is $\ell = 1, 3, 5$ in Eq. (2.12)).

One technical point deserving special attention is the handling of the singularities present in the D^0 propagator in Eq. (2.15). We have taken a finite value $\varepsilon = 0.002\,\omega_{Mie}$ when performing the actual calculations. Our choice modifies slightly ($\sim 5\%$) the width of either the single–particle or the collective plasmon peak. Furthermore, we have summed up all allowed frequency modes for $-2 \leq \{n_u, n_v\} \leq 2$ when calculating D^0. The dynamic polarizability and the total photoabsorption cross section of prolate clusters are mainly dominated by the $n_u = 1$, $n_v = 0, \pm 1$ modes for $M = 0$ and $n_u = 0$, $n_v = 0, \pm 1$ for $M = 1$. However, the oblate cavity presents some peculiar features requiring a finer analysis.

From a theoretical point of view it is interesting to study also the single-particle response (proportional to the imaginary part of the zero-order propagator D^0) since its features are more directly related to the shape of the equilibrium mean field. This can be of help in understanding how this shape affects the collective response.

The effective two-body residual interaction $V(k)$ in Eq.(2.2) determines primarily the position of the collective plasmon peak and, to a lesser extent, its shape. The present semiclassical approach is essentially a Hartree approximation which does not include exchange contributions. However, exchange and correlation terms can be taken into account in a local approximation by introducing a (static) local-field correction $G(k)$ [17]. Thus the momentum-space interaction we use is

$$V(k) = 4\pi\,\frac{e^2}{k^2}\,\left[\,1 - G(k)\,\right]\,, \tag{3.4}$$

with

$$G(k) = A\left[1 - e^{-B\,(k/p_F)^2}\right] , \tag{3.5}$$

where $A = 0.9959$ and $B = 0.2612$ for sodium ([17], p.446) and p_F is the Fermi momentum. In our calculations we have verified that it is possible to take an upper integration limit $k_{max} = 4p_F$ when solving Eq.(2.12) without a noticeable change in the relevant results.

A. Prolate cavity

The natural frequencies $\{\omega_u, \omega_v, \omega_\varphi\}$ of the unperturbed trajectories of particles in the prolate cavity determine the gross behaviour of the semiclassical propagator D^0 (Eq. (2.15)) as a function of ω. Since these frequencies depend on the integration variables ϵ and λ_z it is interesting to evaluate the possible values that they take and their occurrence as a function of the cluster deformation η. In Fig. 1 we show histograms for the probability density of the natural frequencies expressed in terms of the Mie frequency ω_{Mie} and for deformations $\eta = 1.0$, 1.5 and 2. This probability density refers to the occurrence of the frequencies as functions of the (discretized) integration parameters ϵ and λ_z in our numerical calculations. It was evaluated with bins of width $0.002\,\omega_{Mie}$. The frequencies ω_u and ω_φ fall in a narrow range of the order of $0.05\,\omega_{Mie}$, with the former moving to the left and the latter to the right of the spherical limit as deformation increases. For ω_φ we have not plotted the symmetric negative components in Fig. 1. The frequency ω_v shows a different behaviour and it spans, in principle, the $[\sim 0.5\,\omega_{Mie}, \infty]$ range. Overall, Fig. 1 gives a clear idea of the dominant frequency poles contributing to the D^0 propagator.

The $M = 0, 1$ components of the photoabsorption cross section (Eq. (2.21)) per valence electron are shown in Fig. 2 for prolate clusters with deformation ranging from $\eta = 1.0$ to 2., step 0.25. We display the results in a 3–dimensional plot to better assess their relative behaviour. The areas shaded black show the cross section obtained from the zero–order propagator D^0. As a reference, we can observe on the left–hand side of Fig. 2 the same peak corresponding to spherical geometry ($\eta = 1.0$) in both $M = 0$ and 1 components and centered around $\omega \simeq 0.16\,\omega_{Mie}$. Then, the $M = 0$ component shows a photoabsorption peak shifted to lower frequencies as deformation increases. This is a consequence of ω_u (see Fig. 1) determining the dominant pole. The corresponding strength of the peak increases for $\eta = 1$ to ~ 1.5 and then slowly starts to decrease. The $M = 1$ peak is shifted to higher frequencies due to the dominance of ω_φ in this mode and its strength decreases with increasing deformation.

The right–hand side of Fig. 2 shows the partial collective cross sections (shaded gray) evaluated from the full propagator D in Eq. (2.20). By including the fluctuation of the mean field we obtain two main effects: a huge shift in the position of the M component of the photoabsorption peak to frequencies around the Mie frequency and a noticeable change both in the width and the strength of the peak, mainly for $M = 1$. We have numerically checked that the energy–weighted sum rule (area under the curves) is unchanged within 2%. The low–energy collective plasmon ($M = 0$ component) has an intrinsic structure which is slightly more complex than the corresponding high–energy plasmon ($M = 1$ component) and showing some degree of fragmentation noticeable at $\eta \sim 1.5$. The dominant collective peaks in Fig. 2 are slightly blue shifted with respect to the positions predicted by the Mie theory both for the $M = 0$ and 1 components. This completely classical theory predicts that the $M = 0$ and $M = 1$ peaks should be at the frequencies ω_i corresponding to oscillations along the i-axis (z for $M = 0$, x and y for $M = 1$). These frequencies are given by

$$\omega_i = \sqrt{n_i}\, \omega_p \, , \tag{3.6}$$

with n_i the appropriate depolarizing factor. For spherical symmetry $n_x = n_y = n_z = \frac{1}{3}$, giving Eq. (3.1), while for a prolate spheroid [18]

$$n_x = n_y = \tfrac{1}{2} \left(1 - n_z\right) \, , \tag{3.7}$$

$$n_z = \frac{1 - e^2}{2e^3} \left[\log \left(\frac{1 + e}{1 - e} \right) - 2e \right] \, . \tag{3.8}$$

The eccentricity e is related to our deformation parameter η by

$$e = \sqrt{1 - \tfrac{1}{\eta^2}} \, . \tag{3.9}$$

A simple calculation gives $\omega_{x,y} = 1.073\, \omega_{Mie}$, $\omega_z = 0.836\, \omega_{Mie}$ for $\eta = 1.5$ and $\omega_{x,y} = 1.113\, \omega_{Mie}$, $\omega_z = 0.722\, \omega_{Mie}$ for $\eta = 2$. From Fig. 2 we observe that our collective plasmon peaks are blue shifted by $\sim 7\%$ with respect to the position expected from the classical values.

B. Oblate cavity

We turn now to present our results for oblate sodium clusters. One of the most interesting aspects of the present cavity model is the existence of two kinds of three-dimensional orbits, W and B orbits, for oblate geometry (see Appendix). This feature should be shared, at least qualitatively, by more realistic deformed mean fields. In order to estimate the relative importance of the two kinds of orbits, we have plotted in Fig. 3 the fraction of valence electrons following each of the orbits as a function of the cluster deformation η. In the spherical limit, $\eta \to 1$, the cavity only allows W–type three–dimensional orbits since the B orbits become oscillations along a diameter. As deformation increases the fraction of electrons in B orbits raises quickly reaching 50% for $\eta \simeq 1.7$. The presence of W and B orbits in the oblate cavity suggests that we may expect a richer behaviour of the cluster response.

The W and B orbits are characterized by their respective fundamental frequencies (Eq. (2.5)) which in turn determine the D^0 propagator. We shall refer to them as the $\{\omega^W\}$ and $\{\omega^B\}$ frequencies. In order to have an estimate of the possible values they take and of their occurrence for different deformations of the oblate cluster we present histograms for the probability density of the natural frequencies $\{\omega_u^W, \omega_v^W, \omega_\varphi^W\}$ in Fig. 4 and of $\{\omega_u^B, \omega_v^B, \omega_\varphi^B\}$ in Fig. 5. The $\{\omega^W\}$ frequencies in Fig. 4 may be compared to the natural frequencies obtained for the prolate cavity shown in Fig. 1. Clearly the results for $\eta = 1$ in both cases are identical. A great similarity is also observed for ω_v as the clusters get deformed. However, the increasing occurrence of ω_v in Fig. 1 at the lower limit of the frequency range is not present in ω_v^W (Fig. 4). The allowed values for ω_u^W change slightly with deformation and are not sharply defined. The behaviour of ω_u in Fig. 1 is rather different, with the frequency defined in a narrower range and its allowed values decreasing with increasing deformation of the prolate cavity. The ω_φ^W frequency in Fig. 4 shows a similar structure to its counterpart in the prolate case but its magnitude decreases with deformation rather than increasing (Fig. 1).

The $\{\omega^B\}$ frequencies are characterized by a different probability density , as shown in Fig. 5. In the spherical limit ($\eta = 1$) the B orbits have perfectly defined frequencies and $\omega_u^B = \pm\,\omega_\varphi^B = \frac{1}{2}\,\omega_v^B$. As deformation increases ω_u^B becomes much less defined and, on average, takes smaller values than in the spherical case. The frequency ω_φ^B instead is still fairly well defined and is also decreasing with increasing deformation. Furthermore, ω_φ^B shows great similarity with ω_φ^W in Fig. 4. The frequency ω_v^B shows a definitely different behaviour than ω_v^W. It spans a finite range of values depending strongly on the cluster deformation. From the results shown in Figs. 4 and 5 we may expect a more complex behaviour of the D^0 propagator than that observed in the prolate cavity.

The $M = 0, 1$ components of the photoabsorption cross section (Eq. (2.21)) per valence electron are shown in Fig. 6 for oblate clusters with deformation ranging from $\eta = 1.0\,(0.25)\,2.$. As in Fig. 2 we have plotted the cross sections $\sigma_M^{(0)}$ (shaded black) obtained from the propagator D^0 calculated in the static mean field and σ_M (shaded gray) calculated from the correlated propagator D. For $M = 0$ we observe $\sigma_0^{(0)}$ presenting a novel structure. Indeed, the dipole peak is splitted into several peaks as deformation of the oblate cluster increases. A simple estimate based on the probability densities for ω^W and ω^B indicates that both W (dominant) and B orbits contribute to the left most peak in the mode $\{n_u = 1, n_v = 0\}$. At higher frequencies the other two peaks come from B orbits in modes $\{n_u = -1, n_v = 1\}$ and $\{n_u = 1, n_v = 1\}$ respectively. Once fluctuations of the mean field are taken into accout, we obtain a rather complex structure for σ_0 (upper gray peaks). As deformation of the cluster sets in, the $M = 0$ component of the collective dipole peak corresponding to the spherical cluster ($\eta = 1.0$) gets fragmented as a consequence of the more complex structure of D^0 in the resonance region. The amount of fragmentation depends on the deformation parameter. The high frequency peak is more fragmented for $1 < \eta < 1.5$, reaching a rather simple structure with a dominant peak for $\eta = 2$. The $M = 1$ component of the photoabsorption cross section shown in Fig. 6 does not present major new features. The $\sigma_1^{(0)}$ shows a dominant peak for each deformation $\{n_u = 0, n_v = 0)$ with W and B orbits contributing in proportion to the number of valence electrons moving in each of them (see Fig. 3). The collective effects shift the σ_1 dipole peak to frequencies below the one corresponding to the spherical cavity as deformation increases.

The position of the dominant peaks can be compared with the predictions of the classical theory. In the oblate case, the ω_i frequencies are still given by Eqs. (3.6)–(3.7) and [18]

$$n_z = \frac{1+e^2}{e^3}\left[\, e - \arctan e \,\right] \,, \tag{3.10}$$

with the eccentricity e related to our oblate deformation parameter by

$$e = \sqrt{\eta^2 - 1}\,. \tag{3.11}$$

A simple calculation gives $\omega_{x,y} = 0.912\,\omega_{Mie}$, $\omega_z = 1.157\,\omega_{Mie}$ for $\eta = 1.5$ and $\omega_{x,y} = 0.842\,\omega_{Mie}$, $\omega_z = 1.258\,\omega_{Mie}$ for $\eta = 2$. The $M = 1$ collective plasmons (ω_x, ω_y) are again blue shifted and in roughly the same amount we observed in the prolate case ($\sim 7\%$). However for $M = 0$ the collective peaks are now blue shifted by $\sim 10 - 15\%$ with respect to the position expected from the classical values.

C. Comparison between prolate and oblate clusters

In this section we compare the most prominent features concerning the dipole response of spheroidal clusters to an external field. We have chosen to show the photoabsorption cross section per valence electron ($N = 254$) calculated for a sodium cluster which has been deformed to both prolate and oblate shapes. We display calculations corresponding to deformations $\eta = 1.0\,(0.25)\,2$ in both geometries. In Fig. 7 we plot the corresponding cross sections calculated both in the static mean field (single–particle approximation, shaded black) and including collective effects (shaded gray). Arrows are plotted as reference. They place the position of the plasmon peak for a spherical cluster in the present model. For prolate geometry the photoabsorption strenght always displays the characteristic splitting into two pronounced peaks, corresponding to oscillations along two perpendicular symmetry axes ($M = 0$ and $M = 1$). The relative strength of the two collective peaks varies with an increasing dominance of the $M = 1$ component for larger deformations. For oblate spheroidal geometry instead, an interesting phenomenon occurs: one peak dominates the cross section in the $\eta = 1 \div 2$ range. The high–energy collective plasmon ($M = 0$ component) gets fragmented and distributed over an interval of frequencies of the order of $\sim 0.3\ \omega_{Mie}$. This fragmentation tends to dissapear at the largest deformation studied here ($\eta = 2$). However, as shown in Fig. 6, some residual fragmentation remains at frequencies similar to the characteristic frequency of the low–energy plasmon ($M = 1$ component). The effect has been traced back to the appearance of extra peaks in the "single-particle" $M = 0$ strength, that is related to the existence of two kinds of three-dimensional orbits (W-type and B-type) in an oblate cavity. It is reasonable to expect that a similar effect should occur also for more realistic mean fields.

Overall our results give a clear indication on the gross features to be expected for either prolate or oblate medium size sodium clusters. The photoabsorption cross section is splitted into two peaks for the prolate geometry, but is mainly dominated by a single peak in the oblate case for the range of deformations studied here, the smaller peak being further splitted or fragmented.

D. Scaling properties

In this section we investigate the dependence of our results from the valence electron number N and from the density parameter r_s. By using the explicit expressions of the free propagator D^0 given in Sect.II and in the Appendix it is possible to define for each geometry (prolate, oblate, spherical), at given cluster deformation η, a corresponding universal propagator $d^0(\mathbf{x}', \mathbf{x}, s)$ such that

$$D^0(\mathbf{q}', \mathbf{q}, \omega) = N\, {r_s}^2\, d^0(R\mathbf{q}', R\mathbf{q}, \frac{\omega}{\omega_F})\,, \tag{3.12}$$

where $\omega_{_F} \equiv \frac{\pi p_F}{mR}$ and R is the cluster radius for spherical geometry. In Eq.(3.12) all the dependence from the number of valence electrons and from the electron density has been extracted from the free propagator D^0 by relating it to a universal function d^0 of the dimensionless parameters $\mathbf{x} = R\mathbf{q}$ and $s = \frac{\omega}{\omega_{_F}}$. The question we address now is whether a similar factorization occurs also for the collective propagator D. In general this factorization is not possible for an arbitrary interaction V. Indeed, by defining a function $d(\mathbf{x}', \mathbf{x}, s)$ from the collective propagator D through Eq. (3.12) then the integral equation (2.2) leads to the following integral equation for d,

$$d(\mathbf{x}', \mathbf{x}, s) = d^0(\mathbf{x}', \mathbf{x}, s) + \frac{1}{(2\pi)^3 \, r_s} \int d\mathbf{y} \, d^0(\mathbf{x}', \mathbf{y}, s) \, V(\frac{y}{R}) \, d(\mathbf{y}, \mathbf{x}, s) \, , \tag{3.13}$$

which explicitly contains the density parameter r_s. An additional N and r_s dependence is implicit through the R parameter in the force V. Consequently it is not possible to determine an obvious scaling law allowing for the calculation of a universal collective function $d(\mathbf{x}', \mathbf{x}, s)$.

In our case V corresponds to a modified Coulomb–type residual interaction (Eq. (3.4)). Then it is reasonable to search for additional properties of Eq. (3.13) in the presence of a pure Coulomb force. We obtain

$$d(\mathbf{x}', \mathbf{x}, s) = d^0(\mathbf{x}', \mathbf{x}, s) + \frac{1}{(2\pi)^3} \, r_s \, N^{\frac{2}{3}} \int d\mathbf{y} \, d^0(\mathbf{x}', \mathbf{y}, s) \, \frac{4 \, \pi \, e^2}{y^2} \, d(\mathbf{y}, \mathbf{x}, s) \, . \tag{3.14}$$

In this limiting case, the solution to Eq. (3.14) depends on the product $r_s \, N^{\frac{2}{3}}$ only. Deviations from this result are due to more realistic effective interactions and they may be expected to be important in the smaller clusters.

In the limit of large N our microscopic calculations tend to reproduce the results of the macroscopic theory, with the plasmon frequency depending only on the electron density, but not on the total electron number N. The N-dependence of Eq.(3.14) is not in conflict with this expectation since the dimensionless parameter s is related to the frequency by an N-dependent relation $s \propto N^{\frac{1}{3}} \, r_s^2 \, \omega$.

Our discussion indicates that no exact scaling is to be expected for the photoabsorption cross sections in the present model. The actual amount of scaling violation in D does depend on the size, composition and geometry of the particular cluster considered. In order to illustrate the N-dependence of our results we have calculated the collective response of sodium clusters with 25 atoms, thus changing N by an order of magnitude with respect to the results reported earlier. In Fig. 8 we display the collective response of $N = 25$ sodium clusters (shaded black) together with that for $N = 254$ (shaded gray). For spherical and prolate geometry the $N = 25$ plasmons are blue shifted by $\sim$ 10% with respect to the $N = 254$ results, with the overall peak profile showing a qualitatively similar behaviour in the two cases. The light cluster plasmons are sharper due to a smaller Landau damping. For oblate geometry we notice that the fragmentation of the high-frequency plasmon found for $N = 254$ does not appear for $N = 25$. The fragmentation phenomenon is N-dependent and it disappears for different cluster mass. These results agree with our general statement about the lack of scaling with N of the collective propagator D.

The study of clusters with a larger number of valence electrons ($N > 254$) will not provide much new information since the theory starts approaching the classical limits. We have confirmed this by doing calculations for sodium clusters with $N = 2500$. We observe a red shift with respect to the $N = 254$ case of the order of 3% and no fragmentation of the $M = 0$ peak.

We have investigated also the electron-density dependence of our results. Calculations of the photoabsortion cross section for prolate and oblate sodium and potassium clusters ($r_s = 5$) at $N = 254$ show very similar peak profiles (including fragmentation) when the frequency axis is rescaled with the appropriate value of ω_{Mie}. Although the density of valence electrons was decreased by about a factor 2, these small variations can be understood on the basis of Eq. (3.14) where the relevant parameter ($r_s\, N^{\frac{2}{3}}$) was changed by 25%.

IV. SUMMARY AND CONCLUSIONS

In this paper a semiclassical theory of linear response based on the Vlasov equation [9,10] has been extended to spheroidal systems and then applied to study the peak profile of surface plasmon resonances in medium size deformed atomic clusters. Assuming a spheroidal cavity model to describe both prolate and oblate clusters we have been able to calculate the gross features of the cluster response to an external field of frequency ω as a function of the cluster deformation.

Two main general results emerge from our calculations. One of them refers to the splitting of the collective dipole peak with increasing deformation and to the position of these peaks. On this we have commented at lenght in Sec. III. The other main result is related to the width of the dipole peaks. In the present model the single–particle dipole resonance does display a width which is due to the non linearity of the assumed equilibrium mean field. This single-particle width generates a width in the collective plasmon resonances through a mechanism that is analogous to the Landau damping in homogeneous systems. Our calculated width is not sufficient to reproduce the observed plasmon width. However our width is underestimated since we have included only the first few frequency modes when evaluating D^0 in Eq. (2.3). The neglected terms would increase the imaginary part of D^0 in the region of $\omega \simeq \omega_{Mie}$ and thus increasing the Landau damping. Estimates based on numerical calculations including more modes set this effect at about 20%, which is far from sufficient to explain the observed values. Thus more sophisticated effects, like the possible coupling to surface vibrations [19], should perhaps be taken into account.

The fragmentation of the high–energy plasmon peak for medium size oblate clusters is a definite prediction of the present theory and reflects the existence of nontrivial dynamics. The relative importance of this effect depends on several elements such as the shape and size of the cluster and the strength of the effective interaction.

The normalized cluster dipole response shows no simple scaling properties with N at given density ($r_s = 4$). The position of the plasmon peaks is weakly dependent on N, changing by $\sim 10\%$ in the $25 < N < 2500$ mass region while fragmentation of the high energy component dissapears for light ($N \sim 25$) and heavy ($N \sim 2500$) oblate clusters. On the other hand, no major changes in the photoabsorption profile are observed when density decreases by a factor ~ 2 ($r_s = 5$) for a given number N of valence electrons.

Extensions to this work are clearly welcomed. In particular, a close comparison to experiment is required to asses in detail some of the physics missing in the present model. Nevertheless we have established a solid framework to classically understand the gross features of complicated, intrinsically quantum systems.

ACKNOWLEDGMENTS

A.D. is grateful to Prof. D. M. Brink for useful suggestions. F.A.B. thanks support from FONDECYT grant 1960690, Fundación Andes, INFN and Ministero della Pubblica Istruzione, Italy.

APPENDIX:

In this Appendix we specify the details for the expressions given in Sect. II. The propagator D^0 is determined entirely by the single-particle motion in the equilibrium mean field. The classical motion of a point particle in a spheroidal cavity with perfectly reflecting walls has been studied in Ref. [7] for prolate cavities and in Ref. [8] for both prolate and oblate cavities (see also Refs. [20,21]). The authors of Ref. [8] have pointed out that the three-dimensional motion in a prolate cavity is simpler than that in an oblate cavity. We give first a detailed description for prolate geometry. Then, through a simple transformation, the corresponding results for the oblate shape can be recovered. Furthermore we remark the non trivial differences related to particle motion in the two geometries. Our notation follows closely that of Ref. [7].

1. Prolate cavity

To describe the prolate shape, let us introduce the prolate spheroidal coordinates $\{u, v, \varphi\}$ through their relation to the cartesian coordinates,

$$\begin{aligned} x &= \xi_{_P} \cos u \sinh v \cos\varphi \,, && -\tfrac{\pi}{2} \le u \le \tfrac{\pi}{2} \,, \\ y &= \xi_{_P} \cos u \sinh v \sin\varphi \,, && 0 \le v \le \infty \,, \\ z &= \xi_{_P} \sin u \cosh v \,, && 0 \le \varphi \le 2\pi \,, \end{aligned} \tag{A1}$$

with

$$\xi_{_P} = \sqrt{c^2 - a^2} \,. \tag{A2}$$

In the last equation c and a are the larger and smaller semiaxes respectively. The two focal points are at $z = \pm\,\xi_{_P}$.

The equilibrium Hamiltonian h_0 can be expressed in terms of the spheroidal coordinates $\{u, v, \varphi\}$ and their conjugate momenta $\{p_u, p_v, p_\varphi\}$ [7,8]. Assuming that particles move in a static cavity of spheroidal shape, represented by a potential energy $\mathcal{V}(v)$, then h_0 is given by

$${h_0}^{(P)}(u, v, \varphi, p_u, p_v, p_\varphi) = \frac{p_u^2 + p_v^2}{2\,m\,\xi_{_P}^2\,(\cosh^2 v - \sin^2 u)} + \frac{p_\varphi^2}{2\,m\,\xi_{_P}^2\,\sinh^2 v \cos^2 u} + \mathcal{V}(v) \,, \tag{A3}$$

for the prolate configuration. The potential energy for sharp walls is

$$\begin{aligned} \mathcal{V}(v) &= 0 && v < v_2^P \,, \\ &= \infty && v \ge v_2^P \,, \end{aligned} \tag{A4}$$

and the v_2^P parameter is determined by the shape of the cavity,

$$\sinh v_2^P = \frac{a}{\xi_{_P}} \,. \tag{A5}$$

The Hamiltonian (Eq. (A3)) is integrable and the particle motion could, in principle, be described in terms of the angle variables $\{\Phi_u, \Phi_v, \Phi_\varphi\}$ and of the three conjugate action integrals

$$I_u = \frac{1}{2\pi} \oint p_u du \,, \qquad I_v = \frac{1}{2\pi} \oint p_v dv \,, \qquad I_\varphi = \frac{1}{2\pi} \oint p_\varphi d\varphi \,. \tag{A6}$$

However, in the spirit of Ref. [9], the following three other constants of the motion $\{E, \epsilon, \lambda_z\}$ can be conveniently used instead of the action integrals. These new constants are: the particle energy E, the separation variable ϵ and the z-component of the particle angular momentum λ_z (which coincides with the action variable I_φ and with the generalized momentum p_φ). The constant of motion ϵ plays a role analogous to the magnitude of the particle angular momentum in the spherical case.

With the help of the Vlasov equation the angle variables can be explicitly expressed in terms of these three constants of the motion $\{E, \epsilon, \lambda_z\}$ and of the spheroidal coordinates $\{u, v, \varphi\}$. The derivation, based on separation of variables in the linearized Vlasov equation, is lengthy but straightforward, hence we do not report all the details here [22].

The generalized momenta $p_{u,v}$ are

$$\begin{aligned} p_u &= \xi_{_P} \sqrt{2mE} \sqrt{\sigma_1^P - U_{_P}(u, \sigma_2^P)} \,, \\ p_v &= \xi_{_P} \sqrt{2mE} \sqrt{V_{_P}(v, \sigma_2^P) - \sigma_1^P} \,. \end{aligned} \tag{A7}$$

The two dimensionless constants of the motion σ_1^P and σ_2^P are defined as in Ref. [7],

$$\sigma_1^P = \frac{\epsilon}{E} \,, \qquad \sigma_2^P = \frac{\lambda_z^2}{2\, m\, E\, \xi_{_P}^2} \,, \tag{A8}$$

and the effective potentials in Eq. (A7) for the u and v coordinates are given by

$$\begin{aligned} U_{_P}(u, \sigma_2^P) &= \sin^2 u + \frac{\sigma_2^P}{\cos^2 u} \,, \\ V_{_P}(v, \sigma_2^P) &= \cosh^2 v - \frac{\sigma_2^P}{\sinh^2 v} \,. \end{aligned} \tag{A9}$$

Particles on three–dimensional orbits move between two confocal ellipsoids with $v_1^P \le v \le v_2^P$ and $u_1^P \le u \le u_2^P$, with $v_{1,2}^P$ and $u_{1,2}^P$ the turning points obtained as solutions to $p_v = 0$ and $p_u = 0$ respectively (see Ref. [7] for details). Introducing the quantities

$$t_\pm^P = \sqrt{\left(\frac{1-\sigma_1^P}{2}\right) \pm \sqrt{\left(\frac{1-\sigma_1^P}{2}\right)^2 + \sigma_2^P}} \,, \tag{A10}$$

these turning points are obtained from

$$\begin{aligned} \cosh(v_1^P) &= \sqrt{1-(t_-^P)^2}\ , \\ \cos(u_2^P) &= t_+^P\ , \qquad\qquad u_1^P = -\,u_2^P\ , \end{aligned} \tag{A11}$$

and v_2^P from Eq. (A5).

It is our purpose here to specify the integration limits in Eq. (2.15), and to derive explicit expressions for the eigenfrequencies $\omega_{u,v,\varphi}$ as well as for the Fourier coefficients $Q^{(LM)}_{n_u,n_v,n_\varphi}$ appearing in the expression for D^0.

To obtain the integration range for the constant of motion ϵ we realize that the turning point u_2^P exists only if $\cos u_2^P \leq 1$ in Eq. (A11). Also the presence of an infinite potential barrier at the surface of the cavity implies $p_v(v_2^P) = 0$. These two conditions impose constraints on σ_1^P,

$$\begin{aligned} \left(\sigma_1^P\right)_{min} &= \sigma_2^P\ , \\ \left(\sigma_1^P\right)_{max} &= \cosh^2 v_2^P - \frac{\sigma_2^P}{\sinh^2 v_2^P}\ . \end{aligned} \tag{A12}$$

These constraints determine the integration range for ϵ. Thus,

$$\int d\epsilon \quad \longrightarrow \quad \int_{\epsilon_-}^{\epsilon_+} d\epsilon\ , \tag{A13}$$

with

$$\epsilon_- = \frac{\lambda_z^2}{2\,m\,\xi_P^2}\ , \qquad \epsilon_+ = E_F\,\cosh^2 v_2^P - \frac{\epsilon_-}{\sinh^2 v_2^P}\ . \tag{A14}$$

The integration range for the constant of motion λ_z is determined from the possible values of the particle angular momentum along the symmetry axis. Thus,

$$\int d\lambda_z \quad \longrightarrow \quad \int_{\lambda_-}^{\lambda_+} d\lambda_z\ , \tag{A15}$$

where

$$\lambda_\pm = \pm\,(p_F a)\ , \tag{A16}$$

with p_F the Fermi momentum associated to the Fermi energy E_F.

The evaluation of the Fourier coefficients in Eq. (2.17) can be simplified by noticing that

$$n_u\Phi_u + n_v\Phi_v + n_\varphi\tilde{\Phi}_\varphi = s_{\mathbf{n}}(u) + s'_{\mathbf{n}}(v)\ . \tag{A17}$$

The phases $s_{\mathbf{n}}(u)$ and $s'_{\mathbf{n}}(v)$ are given by

$$\begin{aligned} s_{\mathbf{n}}(u) &= \mathbf{n}\cdot\boldsymbol{\omega}\,\tau_u(u) + \mathbf{n}\cdot\mathbf{\Omega}\,\alpha_u(u) - n_\varphi\gamma_u(u)\ , \\ s'_{\mathbf{n}}(v) &= \mathbf{n}\cdot\boldsymbol{\omega}\,\tau_v(v) + \mathbf{n}\cdot\mathbf{\Omega}\,\alpha_v(v) - n_\varphi\gamma_v(v)\ . \end{aligned} \tag{A18}$$

with $\boldsymbol{\omega}$ the frequency vector defined in Eq. (2.5), $\mathbf{\Omega}$ an auxiliary frequency vector and the auxiliary functions $\{\,\alpha_{u,v}, \tau_{u,v}, \gamma_{u,v}\,\}$ given by

$$\begin{aligned}
\alpha_u(u) &= m\,\xi_{_P}^2 \int_{u_{min}}^{u} \frac{du\,'}{p_u(u\,')}\,, & \alpha_v(v) &= -\,m\,\xi_{_P}^2 \int_{v_{min}}^{v} \frac{dv\,'}{p_v(v\,')}\,, \\
\tau_u(u) &= -\,m\,\xi_{_P}^2 \int_{u_{min}}^{u} \frac{\sin^2 u\,'}{p_u(u\,')} du\,'\,, & \tau_v(v) &= m\,\xi_{_P}^2 \int_{v_{min}}^{v} \frac{\cosh^2 v\,'}{p_v(v\,')} dv\,'\,, \\
\gamma_u(u) &= \lambda_z \int_{u_{min}}^{u} \frac{du\,'}{\cos^2 u\,' p_u(u\,')}\,, & \gamma_v(v) &= \lambda_z \int_{v_{min}}^{v} \frac{dv\,'}{\sinh^2 v\,' p_v(v\,')}\,.
\end{aligned} \tag{A19}$$

In these equations the upper integration limit is a variable while the lower one is the corresponding inner turning point for the geometry under study. For the prolate case $u_{min} = u_1^P$ and $v_{min} = v_1^P$. All the integrals appearing in Eq. (A19) can be easily expressed in terms of elliptic integrals and evaluated numerically.

The natural frequencies of the unperturbed trajectories are the three components of the frequency vector $\boldsymbol{\omega}$ (Eq. (2.5)). They can be expressed in terms of these integrals as

$$\begin{aligned}
\omega_u(E,\epsilon,\lambda_z) &= \pi\, \frac{-\,\alpha_v(v_2^P)}{[\,\alpha_u(u_2^P)\tau_v(v_2^P) - \alpha_v(v_2^P)\tau_u(u_2^P)\,]}\,, \\
\omega_v(E,\epsilon,\lambda_z) &= \pi\, \frac{\alpha_u(u_2^P)}{[\,\alpha_u(u_2^P)\tau_v(v_2^P) - \alpha_v(v_2^P)\tau_u(u_2^P)\,]}\,, \\
\omega_\varphi(E,\epsilon,\lambda_z) &= \frac{1}{\pi}\left[\,\omega_v\,\gamma_v(v_2^P) + \omega_u\,\gamma_u(u_2^P)\,\right]\,.
\end{aligned} \tag{A20}$$

Correspondingly, the auxiliary frequency vector $\mathbf{\Omega}$ has components

$$\begin{aligned}
\Omega_u(E,\epsilon.\lambda_z) &= -\,\omega_u\,\frac{\tau_v(v_2^P)}{\alpha_v(v_2^P)}\,, \\
\Omega_v(E,\epsilon.\lambda_z) &= -\,\omega_v\,\frac{\tau_u(u_2^P)}{\alpha_u(u_2^P)}\,, \\
\Omega_\varphi(E,\epsilon,\lambda_z) &= \frac{1}{\pi}\left[\,\Omega_v\,\gamma_v(v_2^P) + \Omega_u\,\gamma_u(u_2^P)\,\right]\,.
\end{aligned} \tag{A21}$$

Note that from the expressions given above we can easily obtain the explicit form of the angle variables in terms of the spheroidal coordinates. For example the explicit form of $\Phi_u(u,v)$ can be derived from Eq. (A17) by setting $n_u = 1$, $n_v = 0$, $n_\varphi = 0$. The angle variable Φ_φ takes the form $\Phi_\varphi = \tilde{\Phi}_\varphi(u,v) + \varphi$.

The evaluation of the Fourier coefficients in Eq. (2.17) is made explicit by using the identity

$$\begin{aligned}
&\oint du \oint dv \left|\frac{\partial(\Phi_u,\Phi_v)}{\partial(u,v)}\right| e^{-i(n_u\Phi_u + n_v\Phi_v + n_\varphi\tilde{\Phi}_\varphi)} = \\
&4\int_{u_1^P}^{u_2^P} du \int_{v_1^P}^{v_2^P} dv \left|\frac{\partial(\Phi_u,\Phi_v)}{\partial(u,v)}\right| \cos[s_{\mathbf{n}}(u)]\cos[s'_{\mathbf{n}}(v)]\,,
\end{aligned} \tag{A22}$$

and evaluating the Jacobian,

$$\left|\frac{\partial(\Phi_u,\Phi_v)}{\partial(u,v)}\right| = \left(m\,\xi_{_P}^2\right)^2\,\frac{\omega_u\,\omega_v}{p_u\,p_v}\left[\frac{\tau_u(u_2^P)}{\alpha_u(u_2^P)} - \frac{\tau_v(v_2^P)}{\alpha_v(v_2^P)}\right]\left(\cosh^2 v - \sin^2 u\right). \tag{A23}$$

Then,

$$Q^{(LM)}_{n_u,n_v,n_\varphi} = \delta_{M,n_\varphi} \int_{u_1^P}^{u_2^P} \frac{du}{p_u} \int_{v_1^P}^{v_2^P} \frac{dv}{p_v}\, F(u,v) \cos[s_{\mathbf{n}}(u)] \cos[s'_{\mathbf{n}}(v)] \,, \tag{A24}$$

with

$$\begin{aligned} F(u,v) = {} & i^L \frac{4}{\pi} \left(m\, \xi_P^2 \right)^2 \omega_u\, \omega_v \left[\frac{\tau_u(u_2^P)}{\alpha_u(u_2^P)} - \frac{\tau_v(v_2^P)}{\alpha_v(v_2^P)} \right] \left[\cosh^2 v - \sin^2 u \right] \\ & \times Y_{LM}(\theta(u,v),0)\, j_L(qr(u,v)) \,. \end{aligned} \tag{A25}$$

The radial coordinate r and the polar angle θ can be easily expressed in terms of the (u,v) variables by using the relations (A1).

The present calculation is simpler if parity selection rules are taken into account. These selection rules originate from the fact that the effective potential $U_P(u,\sigma_2^P)$ is an even function of u and as a direct consequence of the spheroidal geometry invariance under the reflection $z \to -z$. Because of this symmetry some of the Fourier coefficients (Eq. (2.17)) vanish. This can be proved by using the following relations,

$$\begin{aligned} s_{\mathbf{n}}(-u) &= n_u \pi - s_{\mathbf{n}}(u) \,, \\ \cos[s_{\mathbf{n}}(-u)] &= (-)^{n_u} \cos[s_{\mathbf{n}}(u)] \,, \\ \cos[\theta(-u,v)] &= -\cos[\theta(u,v)] \quad = \quad \cos[\pi - \theta(u,v)] \,, \\ Y_{LM}(\theta(-u,v),0) &= (-)^{L-M} Y_{LM}(\theta(u,v),0) \,. \end{aligned} \tag{A26}$$

All the remaining factors in (A24) are even functions of u. Then

$$Q^{(LM)}_{n_u,n_v,n_\varphi} = \delta_{M,n_\varphi} [1 + (-)^{n_u+L-M}] \int_{u_0}^{u_2^P} \frac{du}{p_u} \int_{v_1^P}^{v_2^P} \frac{dv}{p_v}\, F(u,v) \cos[s_{\mathbf{n}}(u)] \cos[s'_{\mathbf{n}}(v)] \,, \tag{A27}$$

with $u_0 = 0$. Equation (A27) implies that, for example, for $L = 1$ and $M = 1$ we need to sum only over *even* values of n_u, while for $M = 0$ we must take only *odd* values of n_u. It means also that $D^0_{L'LM} = 0$ unless $(-)^{L'} = (-)^L$.

2. Oblate cavity

The transformation analogous to (A1) for oblate geometry can be obtained from those equations by exploiting the identities

$$\sinh(v \pm i\,\tfrac{\pi}{2}) = \pm\, i \cosh(v) \,, \qquad \cosh(v \pm i\,\tfrac{\pi}{2}) = \pm\, i \sinh(v) \,. \tag{A28}$$

Then the following formal replacements should be made in (A1) to obtain now the relation between the oblate spheroidal coordinates $\{u, v, \varphi\}$ and the cartesian coordinates,

$$\xi_P \longrightarrow i\,\xi_O \,, \qquad\qquad v \longrightarrow v - i\,\tfrac{\pi}{2} \,, \tag{A29}$$

where

$$\xi_O = \sqrt{a^2 - c^2} \,, \tag{A30}$$

is the radius of the focal circle and a is now the largest semiaxis. Applying the same transformation to the kinetic enegy part in Eq. (A3) we obtain the corresponding equilibrium Hamiltonian for an oblate cavity. The potential energy is still given by Eq. (A4), with v_2^P being replaced by v_2^O,

$$\cosh v_2^O = \frac{a}{\xi_O} \,. \tag{A31}$$

Note that this relation can be obtained by applying the transformation (A29) to Eq. (A5).

The generalized momenta $p_{u,v}$ are obtained by applying the transformation (A29) to the expressions in (A7) and by making the replacements

$$\sigma_1^O = 1 - \sigma_1^P \,, \qquad \sigma_2^O = \frac{\lambda_z^2}{2\,m\,E\,\xi_O^2} = -\,\sigma_2^P \,. \tag{A32}$$

The generalized momenta for the oblate cavity are then expressed as

$$\begin{aligned} p_u &= \xi_O\,\sqrt{2mE}\,\sqrt{\sigma_1^O - U_O(u,\sigma_2^O)}\,, \\ p_v &= \xi_O\,\sqrt{2mE}\,\sqrt{V_O(v,\sigma_2^O) - \sigma_1^O}\,, \end{aligned} \tag{A33}$$

with the oblate effective potentials

$$\begin{aligned} U_O(u,\sigma_2^O) &= \cos^2 u + \frac{\sigma_2^O}{\cos^2 u}\,, \\ V_O(v,\sigma_2^O) &= \cosh^2 v + \frac{\sigma_2^O}{\cosh^2 v}\,. \end{aligned} \tag{A34}$$

Of course we still have $p_\varphi = \lambda_z$.

In Ref. [8] it has been pointed out that the effective potentials $U_O(u,\sigma_2^O)$ and $V_O(v,\sigma_2^O)$ for oblate geometry may exhibit a non monotonic behaviour for some range of values of the parameter σ_2^O. As a consequence the phase space of an oblate spheroidal cavity is divided into two parts and there are two kinds of three-dimensional orbits (plus a separatrix that, however, has zero weight in our calculations). For their description we introduce the equivalent to the quantities $t_\pm^P$ in Eq. (A10) for the oblate case,

$$t_\pm^O = \sqrt{\left(\frac{\sigma_1^O}{2}\right) \pm \sqrt{\left(\frac{\sigma_1^O}{2}\right)^2 - \sigma_2^O}}\,, \tag{A35}$$

which are convenient for expressing the turning points. Of course these parameters can be obtained by making the replacement (A32) in Eq. (A10).

We must now distinguish between the two kinds of three–dimensional orbits occurring in the oblate cavity:

- ***B*–orbits**

  For

$$\sigma_2^O < 1 \qquad \text{and} \qquad 2\sqrt{\sigma_2^O} \le \sigma_1^O \le 1 + \sigma_2^O \,, \tag{A36}$$

the orbits always cross the focal circle. These are the orbits with a hyperboloidal caustic of Ref. [8] and they are analogous to the so–called bouncing ball modes. In this case, the equation $p_u = 0$ has four solutions. The accessible region of phase space is $u_1^B \leq u \leq u_3^B$ and $u_4^B \leq u \leq u_2^B$ and with $0 \leq v \leq v_2^O$. For the lower integration limit in the v variable we have to take $v_1^B = 0$ since the equation $p_v = 0$ has no real solution in the interval $[\,0, v_2^O\,]$. The explicit turning points for the u variable are obtained from

$$\begin{aligned} \cos u_2^B &= t_-^O \,, \qquad & u_1^B &= -\,u_2^B \,, \\ \cos u_4^B &= t_+^O \,, \qquad & u_3^B &= -\,u_4^B \,. \end{aligned} \tag{A37}$$

The constraints expressed in Eq. (A36) imply the following integration range for λ_z and ϵ,

$$\int d\lambda_z \quad \longrightarrow \quad \int_{\lambda_-^B}^{\lambda_+^B} d\lambda_z \,, \qquad\qquad \int d\epsilon \quad \longrightarrow \quad \int_{\epsilon_-^B}^{\epsilon_+^B} d\epsilon \,, \tag{A38}$$

with

$$\begin{aligned} &\lambda_\pm^B = \pm\,(p_F\,\xi_o)\,, \\ &\epsilon_-^B = 2\,E_F\sqrt{\sigma_2^O}\,, \qquad \epsilon_+^B = E_F\,(1+\sigma_2^O)\,. \end{aligned} \tag{A39}$$

- W**–orbits**

For

$$\sigma_2^O \geq 0 \qquad \text{and} \qquad \sigma_1^O \geq 1 + \sigma_2^O \,, \tag{A40}$$

the orbits have an ellipsoidal caustic, and they are analogous to the so-called whispering gallery modes. For these orbits $p_u^2 \geq 0$ for $u_1^W \leq u \leq u_2^W$ and $p_v^2 \geq 0$ for $v_1^W \leq v \leq v_2^O$, with the corresponding turning points given by

$$\begin{aligned} \cos u_2^W &= t_-^O \,, \qquad & u_1^W &= -\,u_2^W \,, \\ \cosh v_1^W &= t_+^O \,. \end{aligned} \tag{A41}$$

The integration limits for the constant of motion integrals (cf. Eq. (A38)) are

$$\begin{aligned} &\lambda_\pm^W = \pm\,(p_F a)\,, \\ &\epsilon_-^W = E_F\,(1+\sigma_2^O)\,, \qquad \epsilon_+^W = E_F\left[\cosh v_2^O + \frac{\sigma_2^O}{\cosh v_2^O}\right]\,. \end{aligned} \tag{A42}$$

The integration limit ϵ_+^W is determined by the cavity surface.

The number of particles moving on each kind of orbits can be easily evaluated with an integration over phase space. The total number of valence electrons is

$$N = \int d\mathbf{\Phi}\; d\mathbf{I}\; F(E), \tag{A43}$$

with $F(E)$ given by Eq. (2.6). Clearly, setting $\hbar = 1$,

$$\begin{aligned} N &= 2 \int d\mathbf{I}\, \theta(E_F - h_0(\mathbf{I}))\,, \\ &= 2 \int_0^{E_F} dE \int d\lambda_z \int d\epsilon \left| \frac{\partial(I_v, I_u)}{\partial(E, \epsilon)} \right| \;. \end{aligned} \tag{A44}$$

We can define $N = N_B + N_W$ with $N_B(N_W)$ the number of valence electrons in $B(W)$–orbits respectively and

$$\begin{aligned} N_B &= 2 \int_0^{E_F} dE \int_{\lambda_-^B(E)}^{\lambda_+^B(E)} d\lambda_z \int_{\epsilon_-^B(E)}^{\epsilon_+^B(E)} d\epsilon \left| \frac{\partial(I_v, I_u)}{\partial(E, \epsilon)} \right| \;, \\ N_W &= 2 \int_0^{E_F} dE \int_{\lambda_-^W(E)}^{\lambda_+^W(E)} d\lambda_z \int_{\epsilon_-^W(E)}^{\epsilon_+^W(E)} d\epsilon \left| \frac{\partial(I_v, I_u)}{\partial(E, \epsilon)} \right| \;. \end{aligned} \tag{A45}$$

The limits for the λ and ϵ integrals in these formulae are given by Eqs. (A39) and (A42) where E_F is replaced by E. Since the propagator (2.3) has the same structure of an integral over the classical phase space as N, it is convenient to make a similar distinction between the contribution of the two kinds of orbits. Thus for oblate geometry we write

$$D^0_{L'LM}(q', q, \omega) = B_{L'LM}(q', q, \omega) + W_{L'LM}(q', q, \omega)\,, \tag{A46}$$

with $B_{L'LM}$ and $W_{L'LM}$ still given by Eq. (2.15) but with the corresponding integration limits for each kind of orbit.

The building blocks of the present calculation are the elliptic integrals given by Eq. (A19) for the prolate case. They determine the frequencies (A20–A21), as well as the phases (A18), required in the evaluation of the Fourier coefficients. The analogous expressions for oblate geometry are obtained by applying the transformation (A29) to the prolate formulae. All formulae given for prolate geometry can be translated in the same way for the oblate case. A little extra care should be taken for the u integrals in the case of B–orbits since the double–well structure of the effective potential $U_O(u, \sigma_2^O)$ makes p_u become imaginary in the interval $[u_3, u_4]$. This integration range must be excluded by very definition of classical phase space. Then, the lower integration limit for u in Eq. (A27) becomes $u_0 = u_4^B$ for B–orbits.

REFERENCES

[1] M.Danos, *Nucl.Pys.* **5**,23 (1958)

[2] W.A.de Heer, *Rev.Mod.Phys.* **65**, 611 (1993)

[3] M.Brack, *Rev.Mod.Phys.* **65**, 677 (1993)

[4] M. Koskinen, P.O.Lipas, and M. Manninen, *Zeit.Phys. D* 35 285 (1995)

[5] K.Clemenger, *Phys.Rev.B,* **32**, 1359 (1985)

[6] A.Bohr and B.R.Mottelson, *Nuclear Physics, vol.II*, (W.A.Benjamin, Inc., London, 1975), p. 219

[7] V.M.Strutinsky, A.G.Magner, S.R.Ofengenden, and T. Døssing, *Z. Phys.***A283**, 268 (1977)

[8] R.Arvieu, F.Brut, J.Carbonell, and J.Touchard, *Pys. Rev. A* **35**, 2389 (1987)

[9] D.M.Brink, A.Dellafiore, and M.Di Toro, *Nucl.Phys.* **A456**, 205 (1986)

[10] A.Dellafiore, F.Matera, and D.M.Brink, *Phys. Rev. A* **51**, 914 (1995)

[11] W.Ekardt and Z.Penzar, *Phys.Rev. B* **43**, 1322 (1991);

[12] A.L.Fetter and J.D.Walecka, *Quantum theory of many-particle systems* (McGraw-Hill, New York, 1971), p.558

[13] G.F.Burgio and M.Di Toro, *Nucl.Phys.* **A476**, 189 (1988)

[14] A.Dellafiore and F.Matera, *Phys. Rev. B,* **41**, 3488 (1990);

[15] J.H.Van Vleck, *Pys. Rev.* **24**, 347 (1924)

[16] H.Goldstein, *Classical Mechanics, 2nd ed.* (Addison-Wesley, Reading MA, 1980)

[17] G.D.Mahan,*Many-Particle Physics* (PlenumPress, New York,1981) p.437

[18] L.D.Landau, E.M.Lifshitz, and L.P.Pitaevskii, *Electrodynamics of Continuous Media* (Pergamon Press, Oxford, 1984) p.25

[19] J.M.Pacheco, and R.A.Broglia, *Phys. Rev. Lett.* **62** 1400 (1989)

[20] H. Frisk, *Nucl. Phys.* **A511**, 309 (1990)

[21] H.Nishioka, M.Ohta, and S.Okai, *Mem. Konan Univ.* **38**, 1 (1991); H.Nishioka, N.Nitanda, M.Ohta, and S.Okai, *ibid.* **39**, 67 (1992)

[22] A more detailed derivation is available upon request to della@fi.infn.it

FIGURES

FIG. 1. Probability density for the natural frequencies $\{\omega_u, \omega_v, \omega_\varphi\}$ at different deformations η in the prolate sodium cluster described in text.

FIG. 2. $M = 0, 1$ components of the photoabsorption cross section per valence electron for a prolate cluster at different deformations and both in the "single–particle" (shaded black) and "RPA–type" (shaded gray) approximations.

FIG. 3. Fraction of particles on B (full curve) and W (dotted curve) orbits as a function of deformation η for an oblate sodium cluster.

FIG. 4. Probability density for the natural frequencies $\{\omega_u^W, \omega_v^W, \omega_\varphi^W\}$ characteristic of W orbits at different deformations η in the oblate sodium cluster described in text.

FIG. 5. As in Fig. 4 for natural frequencies characteristic of B orbits.

FIG. 6. As in Fig. 2 for an oblate cluster.

FIG. 7. Photoabsorption cross section per valence electron for prolate and oblate sodium clusters at several deformations. The left–hand side of the figure shows the results obtained in a single–particle approximation ($\sigma^{(0)}$). Arrows indicate position of plasmon peak in the spherical case.

FIG. 8. Photoabsorption cross section per valence electron for prolate and oblate sodium clusters at several deformations and for $N = 25$ (shaded black) and $N = 254$ (shaded gray).

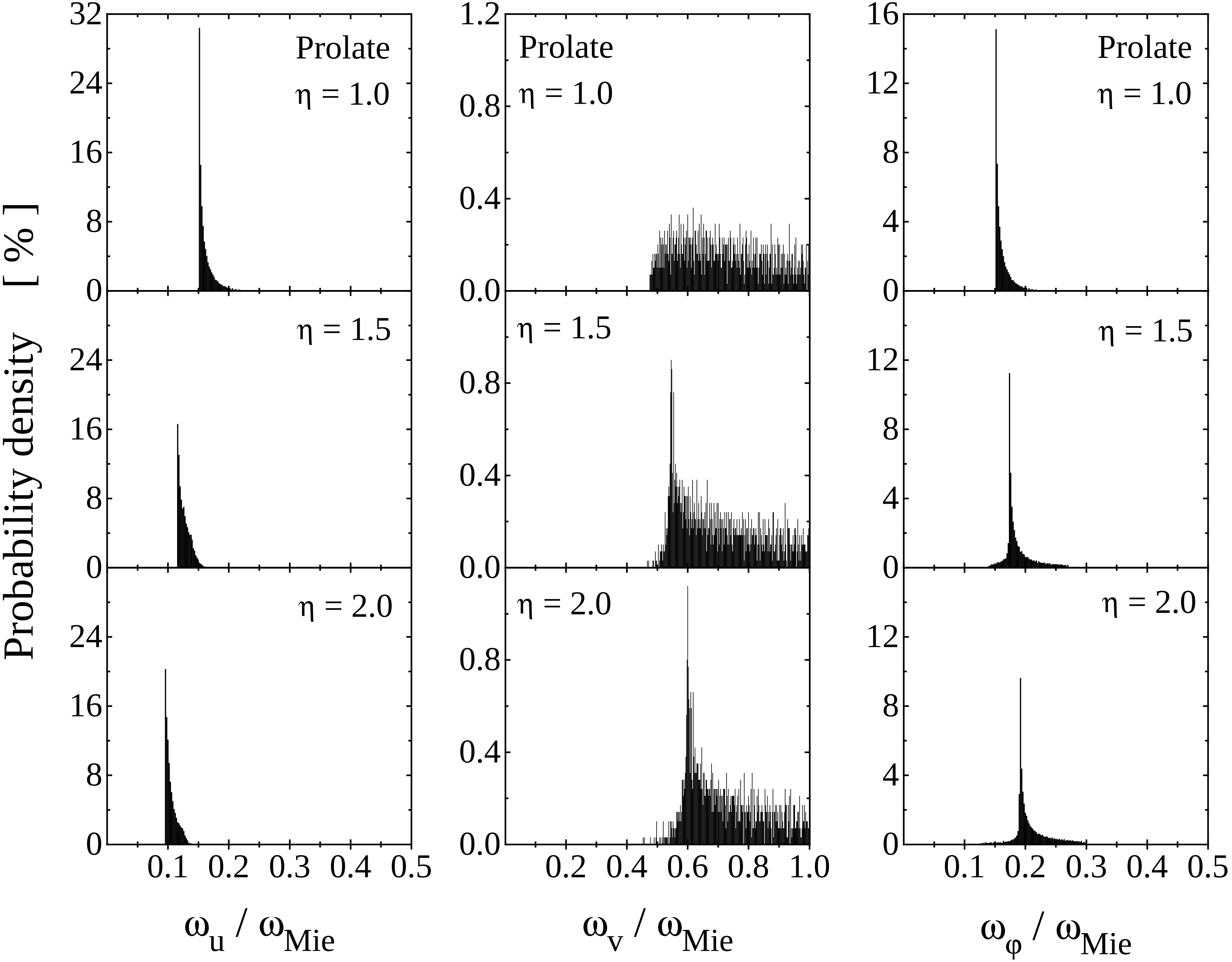

Probability density [%]
Prolate
η = 1.0
η = 1.5
η = 2.0
32
24
16
8
0
1.2
0.8
0.4
0.0
12
4
0.1
0.2
0.3
0.4
0.5
0.6
1.0
ω_u / ω_Mie
ω_v / ω_Mie
ω_φ / ω_Mie

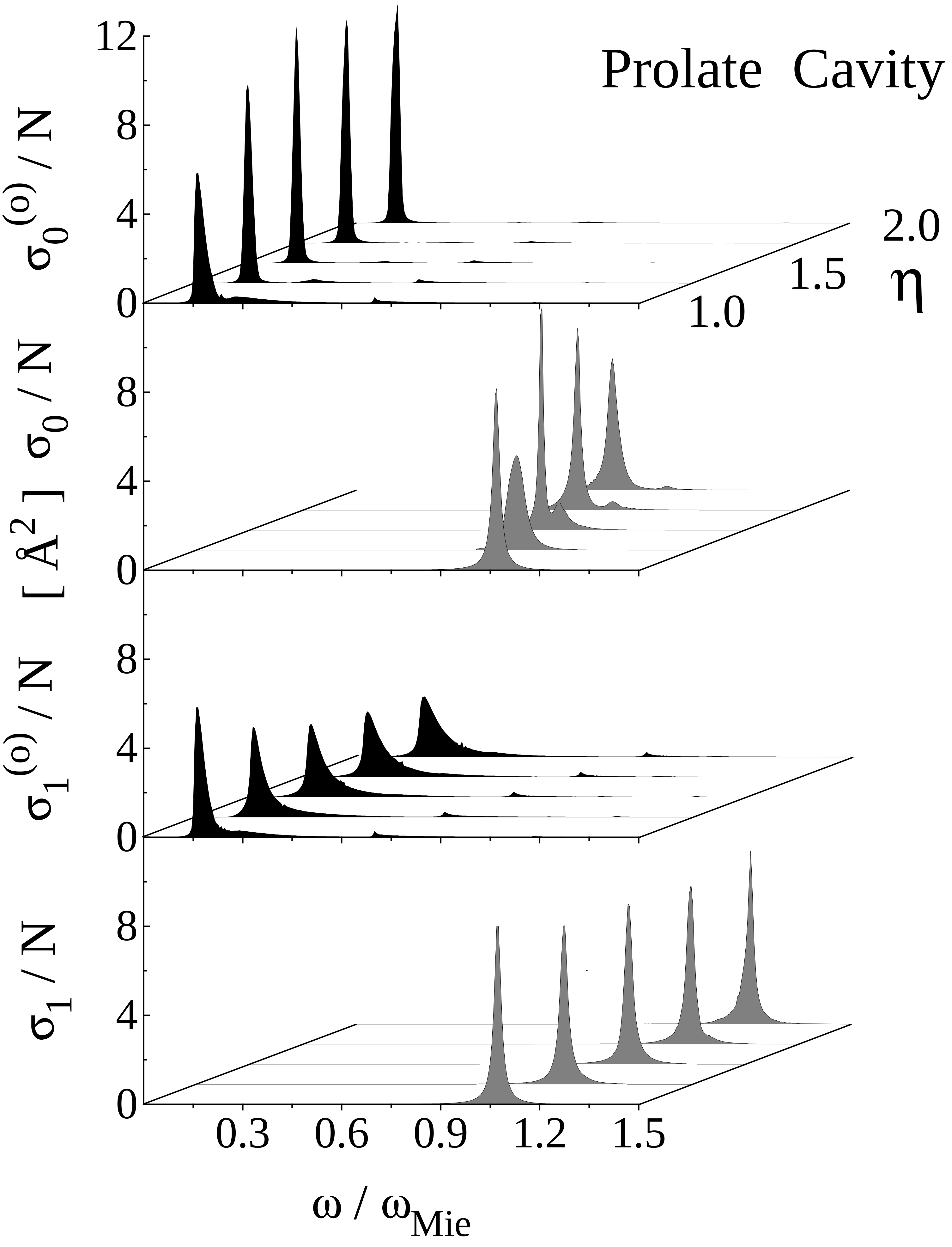
Prolate Cavity
$\sigma_0^{(o)}$ / N
σ_0 / N
[Å^2]
$\sigma_1^{(o)}$ / N
σ_1 / N
0
4
8
12
2.0
1.5
1.0
η
0.3
0.6
0.9
1.2
1.5
ω / ω_{Mie}

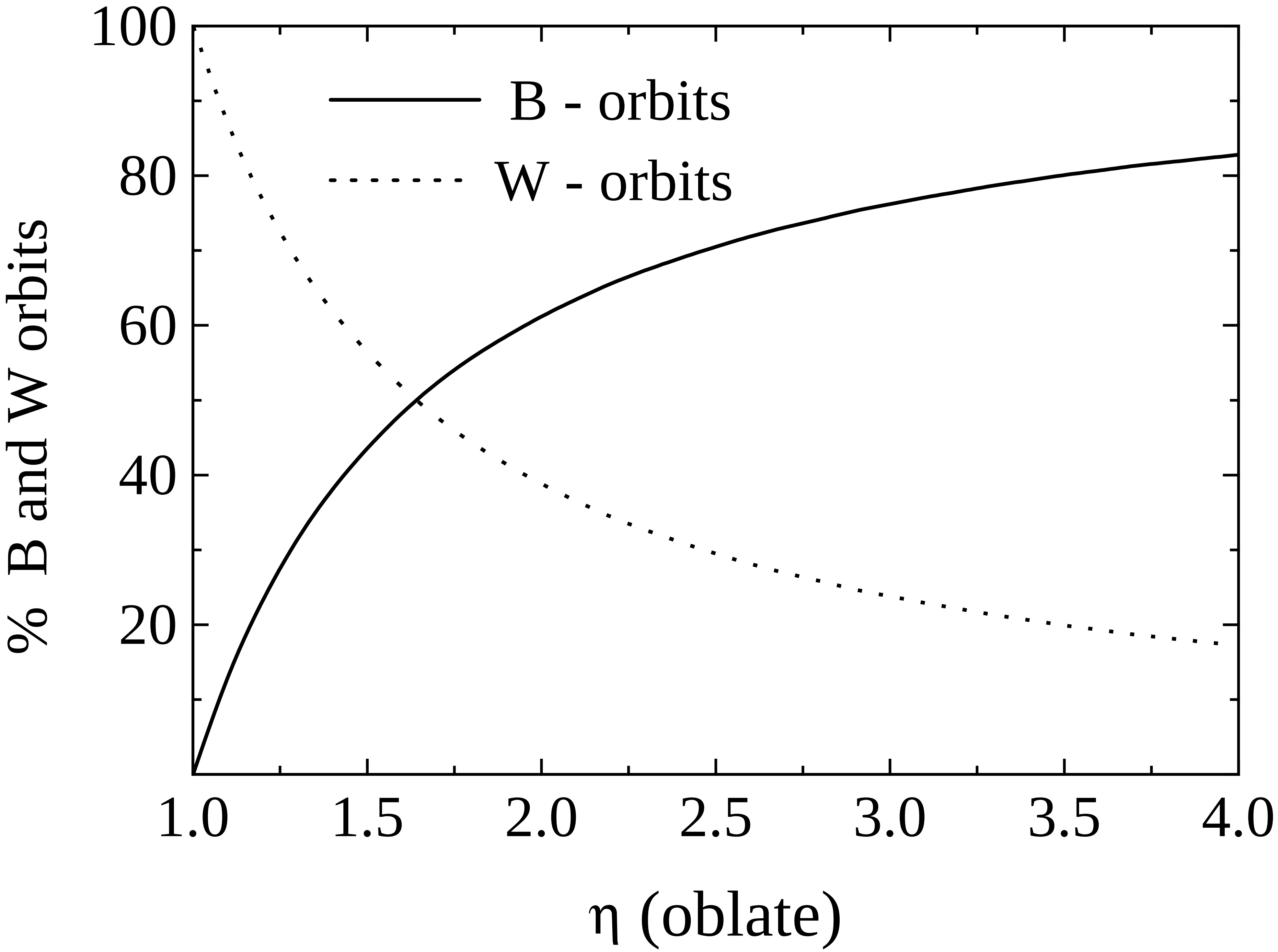
100
80
60
40
20
% B and W orbits
B - orbits
W - orbits
1.0
1.5
2.0
2.5
3.0
3.5
4.0
η (oblate)

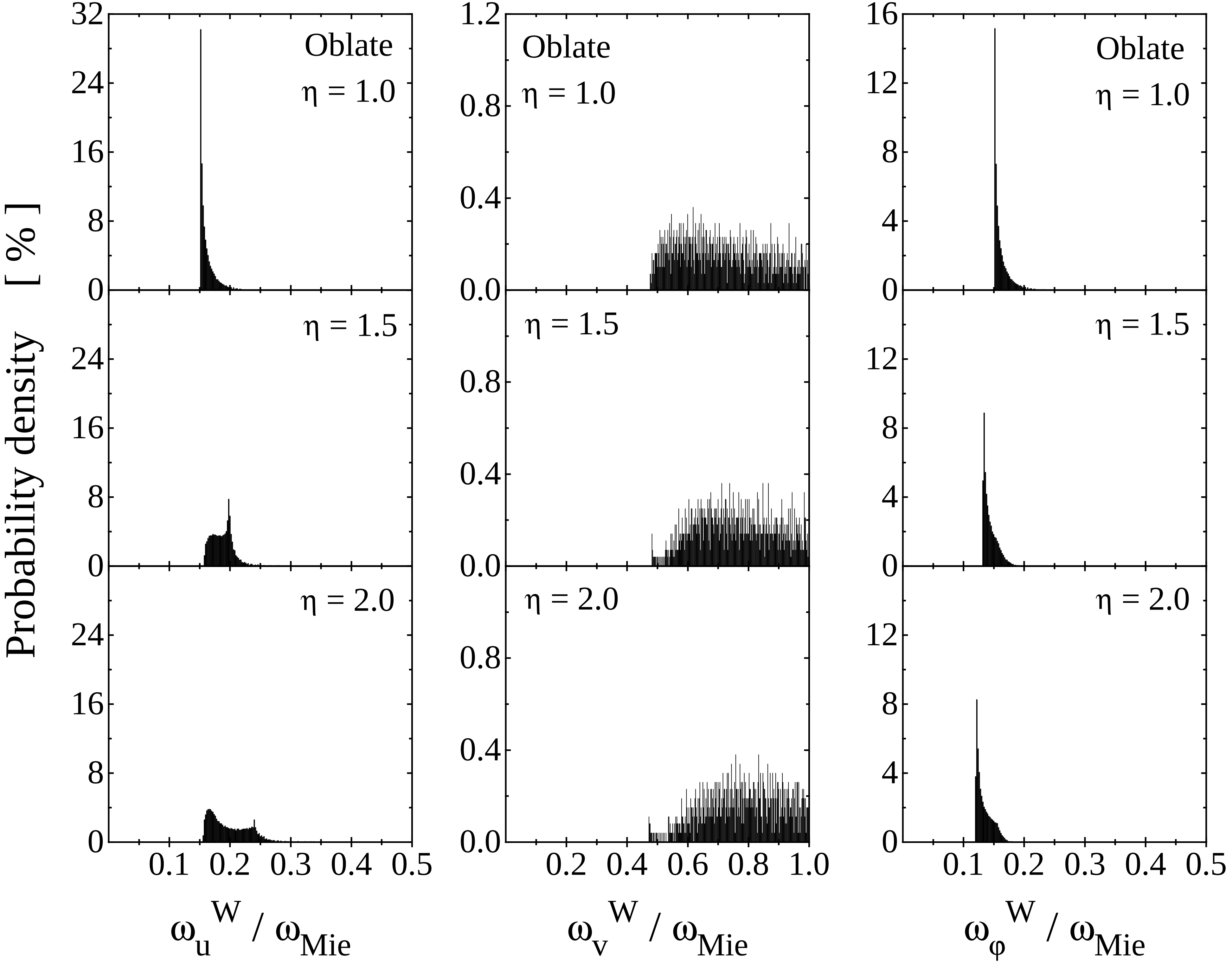
Probability density [%]
Oblate
η = 1.0
η = 1.5
η = 2.0
0
8
16
24
32
0.0
0.4
0.8
1.2
0
4
8
12
16
0.1
0.2
0.3
0.4
0.5
0.2
0.4
0.6
0.8
1.0
$\omega_u^W / \omega_{Mie}$
$\omega_v^W / \omega_{Mie}$
$\omega_\varphi^W / \omega_{Mie}$

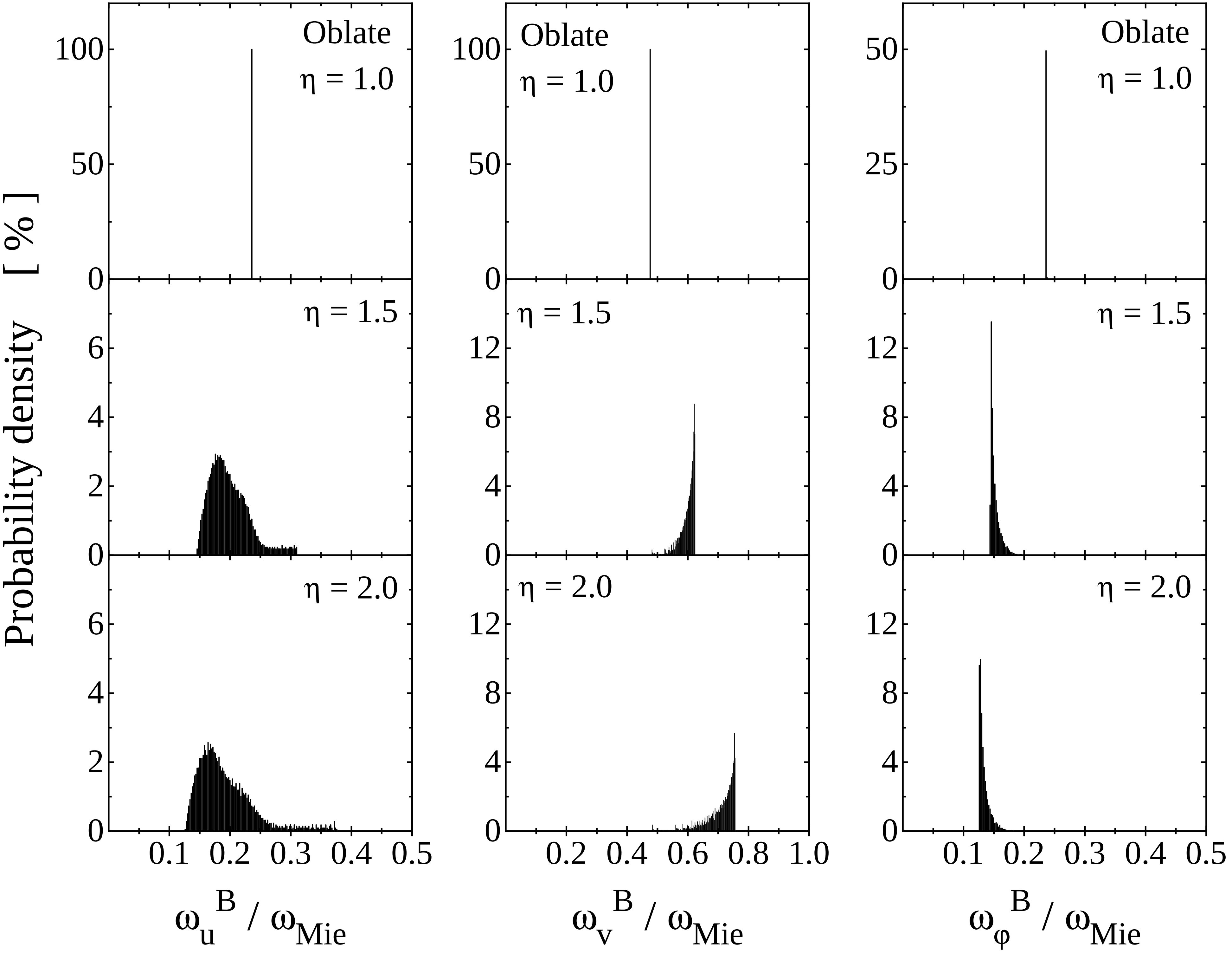

Probability density [%]
Oblate
η = 1.0
η = 1.5
η = 2.0
0
50
100
25
0
2
4
6
8
12
0.1
0.2
0.3
0.4
0.5
0.6
0.8
1.0
$\omega_u^B / \omega_{Mie}$
$\omega_v^B / \omega_{Mie}$
$\omega_\varphi^B / \omega_{Mie}$

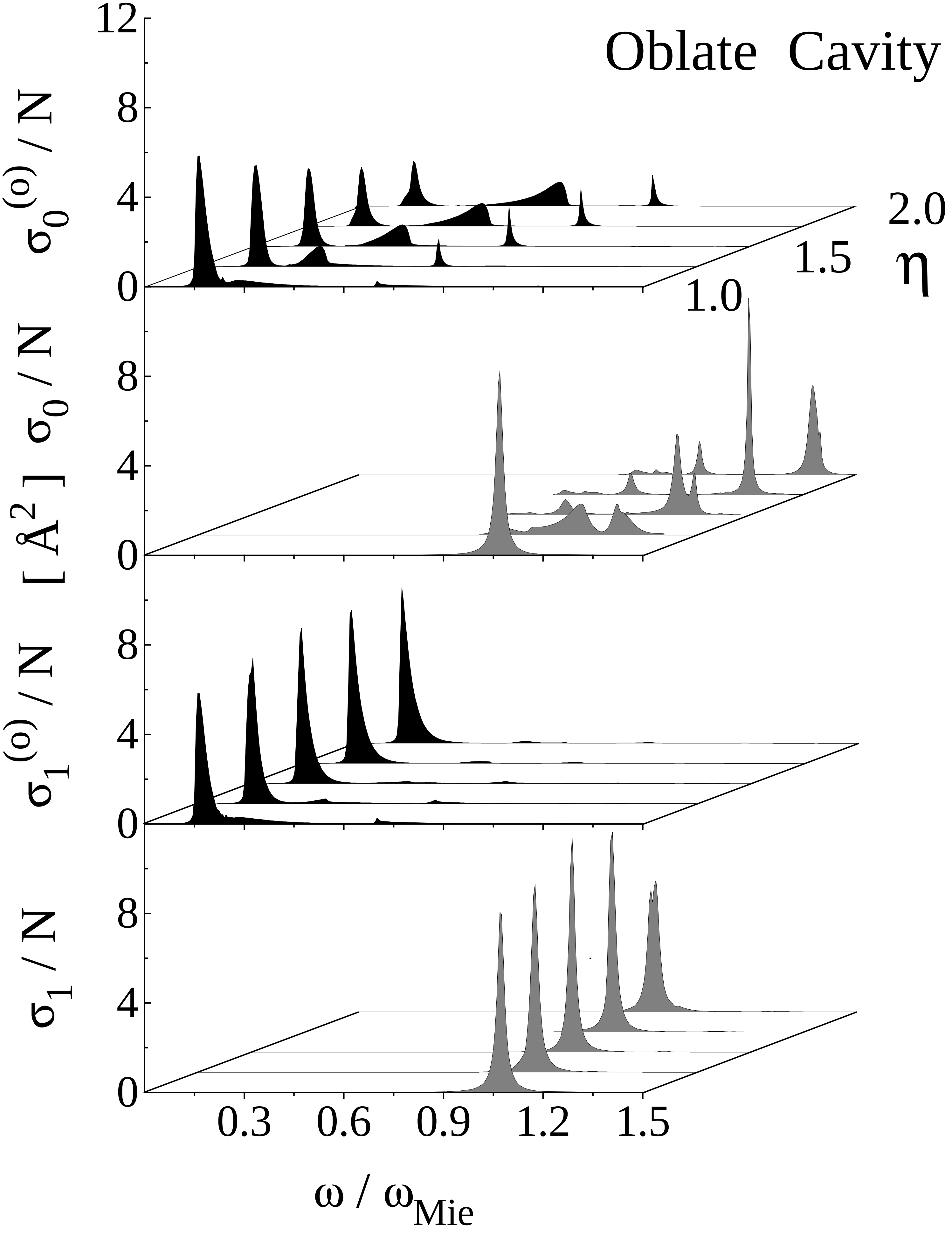
Oblate Cavity
12
8
4
0
$\sigma_0^{(o)}$ / N
2.0
1.5
1.0
η
8
4
0
[Å^2] σ_0 / N
8
4
0
$\sigma_1^{(o)}$ / N
8
4
0
σ_1 / N
0.3
0.6
0.9
1.2
1.5
ω / ω_{Mie}

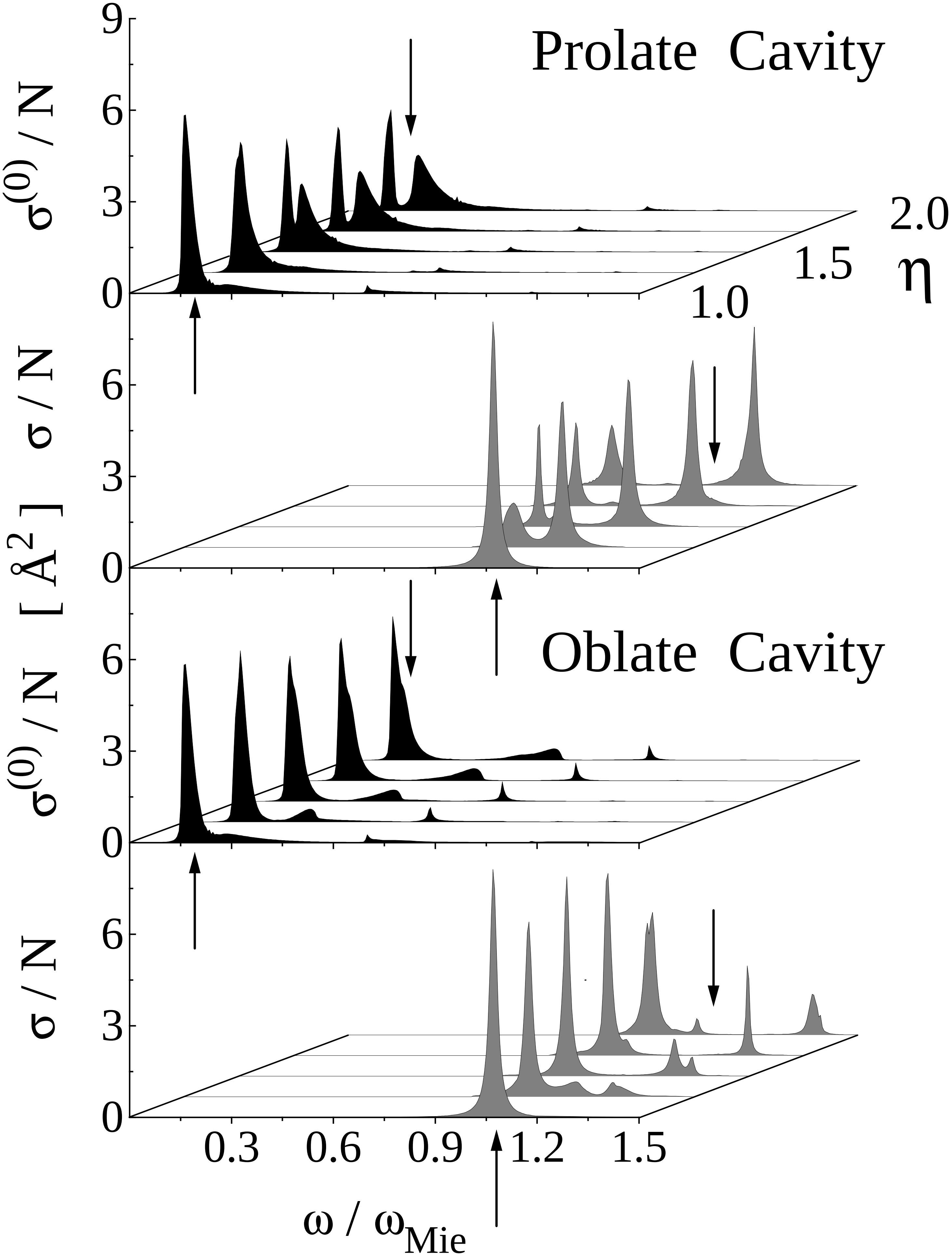
Prolate Cavity
Oblate Cavity
$\sigma^{(0)}$ / N
σ / N
[Å^2]
0
3
6
9
2.0
1.5
1.0
η
0.3
0.6
0.9
1.2
1.5
ω / ω_{Mie}

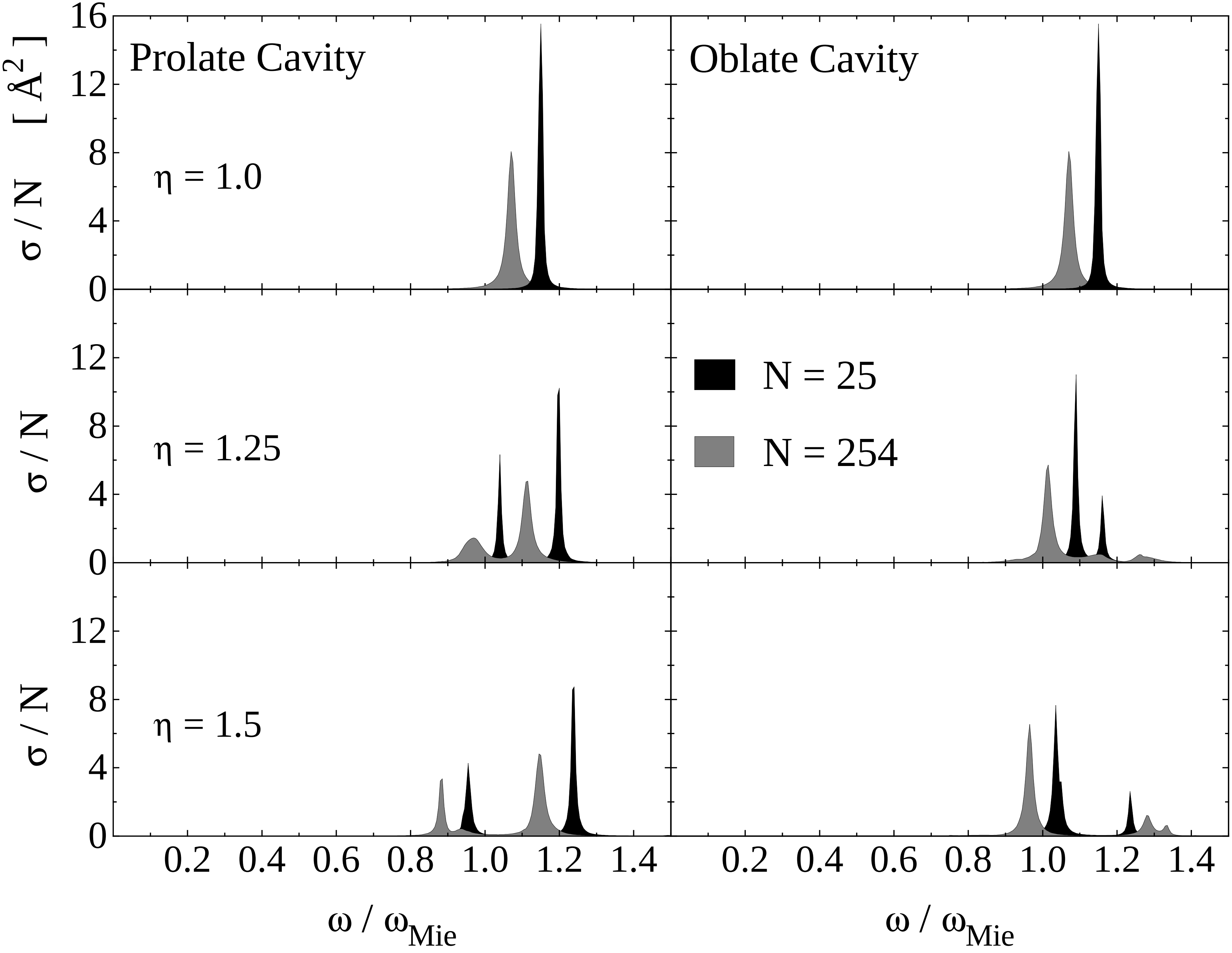
Prolate Cavity
Oblate Cavity
η = 1.0
η = 1.25
η = 1.5
N = 25
N = 254
σ / N [Å^2]
σ / N
σ / N
0
4
8
12
16
0.2
0.4
0.6
0.8
1.0
1.2
1.4
ω / ω$_{Mie}$
ω / ω$_{Mie}$